Hossein Hassanzadeh, Saptarshi Joshi and Seyed Mohammad Taghavi*

Predicting buoyant jet characteristics: a machine learning approach

https://doi.org/10.1515/cppm-2023-0026
Received March 19, 2023; accepted May 18, 2023; published online June 6, 2023

Abstract: We study positively buoyant miscible jets through high-speed imaging and planar laser-induced fluorescence methods, and we rely on supervised machine learning techniques to predict jet characteristics. These include, in particular, predictions to the laminar length and spread angle, over a wide range of Reynolds and Archimedes numbers. To make these predictions, we use linear regression, support vector regression, random forests, K-nearest neighbour, and artificial neural network algorithms. We evaluate the performance of the aforementioned models using various standard metrics, finding that the random forest algorithm is the best for predicting our jet characteristics. We also discover that this algorithm outperforms a recent empirical correlation, resulting in a significant increase in accuracy, especially for predicting the laminar length.

Keywords: buoyant jets; fluid mechanics; laminar length; machine learning; spread angle.

1 Introduction

Injection of a fluid into an ambient fluid of different density typically leads to the formation of a buoyant jet [1]. A positively (negatively) buoyant jet is typically generated when the momentum and buoyancy fluxes act in the same (opposite) direction [2, 3]. Buoyant jets are a frequent occurrence both in the natural world and in industry. In nature, for example, buoyant jets are encountered in volcanic eruptions [4], flows of rivers into oceans and lakes [5], motion of clouds [6] and meteorology [7]. Industrial examples of buoyant jets are many and may include effluent and pollutant releases [8, 9], cleaning processes [10, 11], and building ventilation [12], to name a few.

To understand buoyant jet behaviours, it is essential to examine jet characteristics, which as described in recent studies [13–16], can be classified into two categories based on their temporal behaviour: unsteady and quasi-steady. As an example, the jet penetration length, representing the distance that the jet has traveled at a given moment in time, serves as a model for the unsteady and quasi-steady characteristics in positively and negatively buoyant jets, respectively [2, 16, 17].

A non-buoyant jet, characterized by an absence of a density difference between the jet and surrounding fluid, can be divided into two primary regions: a laminar region and a turbulent region, as established in the classical work of McNaughton and Sinclair [18]. They have found that, following injection and over some distance, the jet initially maintains a stable cylindrical shape with a smooth boundary. However, after a certain distance from the nozzle (known as the laminar length, L_m), the jet begins to become unstable, resulting in visible growing perturbations at its boundary [19]. L_m exhibits several noteworthy features, such as a jet diameter that closely matches that of the nozzle, and energy levels that are near-identical to those of the source [13]. Thanks to the interest in understanding/analyzing L_m, a number of correlations have been developed to predict it, for instance for non-buoyant jets [18, 20, 21], indicating that L_m decreases with an increase in the Reynolds number (Re). For positively buoyant jets, Hassanzadeh et al. [13] have recently extended an empirical correlation for L_m based on Re and Archimedes number (Ar), revealing that L_m increases with an increase in Ar.

***Corresponding author: Seyed Mohammad Taghavi**, Department of Chemical Engineering, Université Laval, Québec, QC, G1V 0A6, Canada, E-mail: Seyed-Mohammad.Taghavi@gch.ulaval.ca. https://orcid.org/0000-0003-2263-0460
Hossein Hassanzadeh and Saptarshi Joshi, Department of Chemical Engineering, Université Laval, Québec, QC, G1V 0A6, Canada

After the laminar length ends, the jet undergoes breakdown and its radius expands while its energy decreases [13, 22]. The jet expansion rate can be quantified via the jet spread angle (θ), i.e., a quasi-steady characteristic that remains nearly constant over time. Non-buoyant jets at high Reynolds numbers typically exhibit a spread angle of approximately $\theta \approx 21°–25°$ [23]. For positively buoyant jets [13], θ decreases with an increase in Re and Ar. Note that an accurate prediction of buoyant jet shapes and boundaries, facilitated by determining L_m and θ, can hold practical significance for environmental and industrial processes, e.g., jet cleanings [24], jet fires [25], environmental flows [26], wastewater discharges [27], drug delivery systems [28], 3D printing technologies [29], and needle-free injections [30].

To properly implement machine learning techniques, it is essential to have high-quality, unbiased, and representative datasets [31–33]. Depending on the available datasets and the desired outcome of applying machine learning, it is beneficial to distinguish between different types of machine learning tasks [34]. For instance, the unsupervised learning technique is tailored for analyzing unlabeled datasets, where the correct responses (labels) are not known, but there is still a need to extract meaning or patterns from the data [35]. On the other hand, the reinforcement learning technique is not employed to learn the patterns in the data, but rather to discover a model of how a given system operates [34]. In addition, the supervised learning is a popular class of machine learning that learns from known (labeled) data to make predictions or decisions about unseen data [36]. In supervised learning, a model is trained on a set of input–output pairs, called training data, where the inputs represent the features of the data and the outputs represent the corresponding labels or targets. There are various supervised learning algorithms that differ in their assumptions, complexity, and ability to handle different types of data. Some popular algorithms include linear regression (LR), random forests (RF), support vector regressions (SVR), K-nearest neighbors (KNN), and artificial neural networks (ANN) [37–39].

In fluid mechanics, data-driven and machine learning modeling are being increasingly explored, e.g., as a potential alternative to revisit existing empirical laws [40]. With the aim to model the relationship between observed data and target variables, supervised learning techniques have been successful in mapping complex non-linear relationships [41, 42], making them suitable for modeling buoyant jets. Unsupervised and semi-supervised learning algorithms [40, 43], designed to uncover hidden structures in datasets, could be also potential methods for modeling jet characteristics, although supervised learning may remain favoured for this task [44, 45]. On the other hand, one could perhaps argue that reinforcement learning [46], which focuses on maximizing reward through sequential actions in a given environment, may not be appropriate for modeling buoyant jets.

In recent years, researchers have turned to machine learning techniques to improve the accuracy of predicting jet flow characteristics, which have long been a subject of interest in fluid mechanics, with broad applications across various industries and environments. For example, El-Amin & Subasi [47] have examined the performance of different supervised learning algorithms to predict the temperature distribution in turbulent jets, involving the injection of hot water into colder ambient. Their analysis has revealed that the RF algorithm outperforms other algorithms in accurately predicting the temperature variation over time. Mashhadimoslem et al. [48] have investigated the jet fires that occur as a result of accidents involving hydrocarbon fuels, such as explosions and fires. They have employed the ANN algorithm trained on literature data to predict both the length of the flame and the released heat flux during the jet fire process. Their results has shown that the ANN algorithm performs well in predicting the hydrocarbon jet fire characteristics, suggesting its potential for use in quantitative risk assessments in industries. Kumar et al. [49] have evaluated various machine learning algorithms to predict the volume oxygen transfer coefficient in plunging jet aerators. Their findings have indicated that the SVR algorithm offers the highest accuracy in estimating this coefficient. In addition, their results have highlighted the significance of the jet velocity as the most influential parameter affecting the oxygenation performance of plunging jets.

Despite the significant role of buoyant jet characteristics in many applications, our brief literature review shows a research gap regarding the prediction of these characteristics using machine learning techniques. To the best of our knowledge, no studies have yet explored the positively buoyant jet features using these techniques, emphasizing the need for further investigations in this research area. Therefore, in this study, we aim to address the lack of research on modeling positively buoyant miscible jet characteristics through the use

of machine learning techniques, in particular, to predict L_m and θ, for a wide range of Re and Ar. We conduct our experiments using high-speed imaging and planar laser-induced fluorescence (PLIF) techniques. Using experimental data, we train multiple supervised learning algorithms, including linear regression (LR), support vector regression (SVR), random forests (RF), K-nearest neighbour (KNN), and artificial neural network (ANN) algorithms. Then, we evaluate the performance of these models using various standard metrics and identify the most accurate predictive model for our flows.

The paper is organized into three sections. The methodology, including the experimental setup, measurement techniques, and machine learning algorithms used in our work, is presented in Section 2. Then, Section 3 provides our experimental results and evaluates the performance of various machine learning algorithms. Finally, the work is briefly summarized in Section 4.

2 Methodology

In this section, we present the details of our experimental setup, procedure, and materials, followed by brief explanations of our measurement techniques, including the high-speed imaging and planar laser-induced fluorescence (PLIF) methods. We then introduce the supervised algorithms employed and present the metrics used to compare their performances.

2.1 Experimental setup and procedure

Our experimental setup, as shown in Figure 1a, included a transparent tank and a centrally located circular nozzle for injecting a heavier fluid (salt-water, coloured with black ink) into a lighter ambient fluid (deionized water). The higher density of the injection fluid was obtained with adding sodium chloride as weighting agent. The tank was filled with the ambient fluid, and the injection fluid was fed by a gear pump (ISMATEC MCP-Z series), providing a wide range of injection velocities, $\hat{V}_0$ (note that we mark the

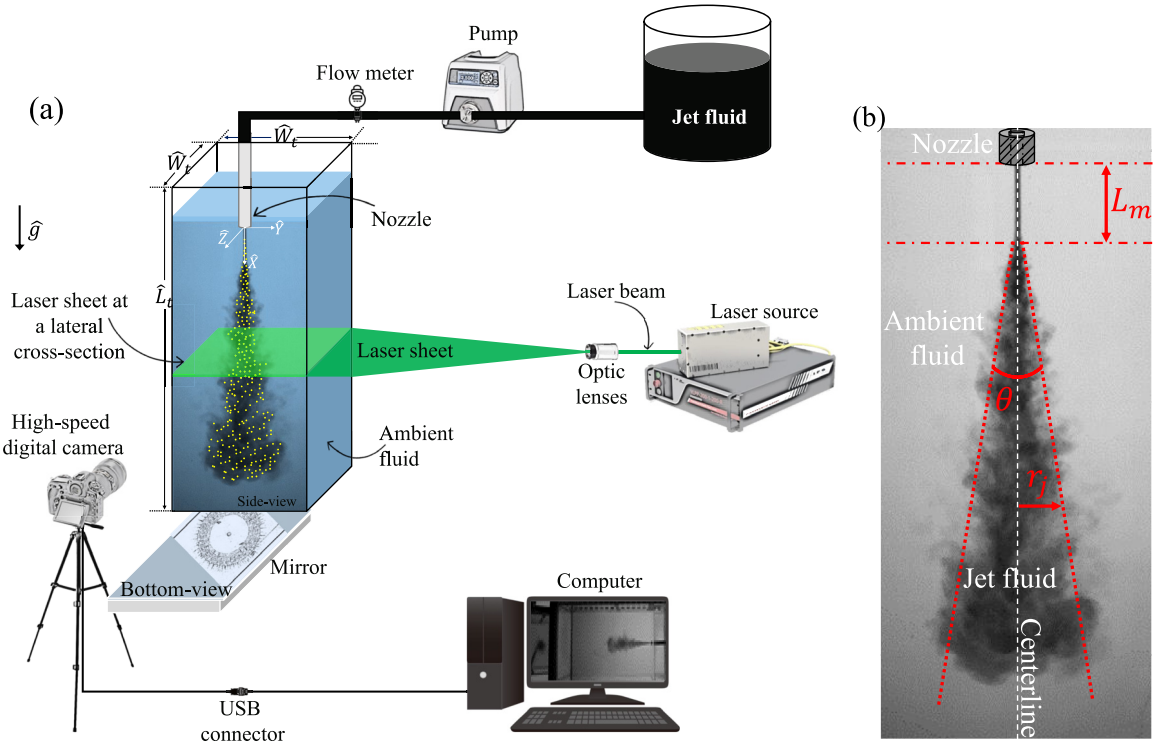

Figure 1: Experimental setup and key characteristics of positively buoyant jets. (a) Experimental setup schematic, including high-speed imaging and PLIF for capturing positively buoyant jet behaviour, with gravity indicated by g . (b) A typical positively buoyant jet formed by injecting a heavy fluid into a transparent fluid, defined by dimensionless laminar length (L_m) and spread angle (θ) with dimensionless jet radius (r_j), and a white dashed centerline.

dimensional parameters with the hat symbol and the dimensionless ones without throughout this manuscript). It should be mentioned that our experimental domain was fairly large ($\widehat{W}_t/\widehat{D}_n$ and $\widehat{L}_t/\widehat{D}_n \gg 1$), allowing us to neglect any potential wall effects on the flow dynamics. In fact, this assumption enabled us to treat the jet as flowing through an unbounded environment, also known as a free jet. Table 1 outlines the dimensions of the rectangular tank and the range of flow parameters used in this study.

Our main jet flow features (i.e., laminar length and spread angle) were extracted through image analysis of high-speed camera recordings. These recordings were made using a low-noise high-speed digital camera (Basler acA2040-90µm), capturing images at regular intervals (typically 20 frames per second or higher if needed). The setup was illuminated behind, top and sides via light boxes (containing light-emitting diode series); this light was filtered through diffusive sheets for homogeneity. The light intensities were converted to normalized concentration maps, via in-house MATLAB codes, based on two reference images taken for the light absorption calibrations. Finally, the jet features of our interest were inferred from the jet boundary obtained through the normalized concentration images.

PLIF was used to visualize 2D (bottom view) cross-sections of our jets. The process involved illuminating a cross-section of the flow with a green laser sheet (Laserglow technologies, wavelength of 532 nm) after dyeing the heavier injected fluid with fluorescent particles (i.e., rhodamine B). The illuminated cross-section was captured by a high-speed digital camera, positioned below the setup perpendicular to the laser sheet plane, allowing us to capture of the bottom-view flow structures.

We gain a deeper understanding of the physics underlying the jet flow dynamics by exploring the role of main governing dimensionless numbers, i.e., the Reynolds and Archimedes numbers [13]. The Reynolds number represents the ratio of inertial force to viscous force and is given by:

$$\mathrm{Re} = \frac{\widehat{\rho}_m\, \widehat{V}_0\, \widehat{D}_n}{\widehat{\mu}_\mathrm{j}} \tag{1}$$

where $\widehat{\rho}_m$ is the averaged density (i.e., $\widehat{\rho}_m = \frac{\widehat{\rho}_\mathrm{j}+\widehat{\rho}_\mathrm{a}}{2}$), $\widehat{V}_0$ is the injection flow velocity, $\widehat{D}_n$ is the nozzle diameter, and $\widehat{\mu}_\mathrm{j}$ is the jet viscosity. On the other hand, the Archimedes number reflects the ratio of buoyant force to viscous force, defined as:

$$\mathrm{Ar} = \frac{\widehat{\rho}_m\,(\widehat{\rho}_\mathrm{j} - \widehat{\rho}_\mathrm{a})\widehat{g}\,\widehat{D}_n^3}{\widehat{\mu}_\mathrm{j}^2}, \tag{2}$$

where $\widehat{g}$ represents the acceleration due to gravity. In the current study, we investigate the dynamics of our buoyant jets for a wide range of dimensionless numbers, i.e., $8\times10^2 \lesssim \mathrm{Re} \lesssim 14\times10^3$ and $10^2 \lesssim \mathrm{Ar} \lesssim 6\times10^5$. Furthermore, to extend the applicability of our results across diverse conditions and scales, we make all lengths, times, and velocities dimensionless using characteristic parameters obtained by balancing the source momentum and volume fluxes [2]. We achieve this by employing $\widehat{D}_n$, $\frac{\widehat{D}_n}{\widehat{V}_0}$, and $\widehat{V}_0$ to make lengths, times, and velocities dimensionless, respectively. Therefore, throughout the paper and unless otherwise stated, all quantities are rendered dimensionless, to ensure a consistent and comprehensive approach to our analysis.

2.2 Machine learning techniques

In the present study, our focus is on supervised learning algorithms, due to the availability of labeled data and our goal of accurately predicting buoyant jet characteristics. As mentioned before, the supervised learning technique relies on labeled data with known target values, making it a suitable choice for our available data. In addition, for the purpose of an accurate prediction, the supervised learning

Table 1: The values and ranges of the dimensional flow parameters in our study. Note that the properties of the jet and ambient fluids are distinguished by the subscripts "j" and "a", respectively.

Parameter	Name	SI unit	Range or value
$\widehat{D}_n$	Nozzle diameter	M	$(1.6\text{–}3.6)\times10^{-3}$
$\widehat{g}$	Gravitational acceleration	$\frac{\mathrm{m}}{\mathrm{s}^2}$	9.81
$\widehat{L}_t$	Tank length	M	4×10^{-1}
$\widehat{V}_0$	Mean injection velocity	$\frac{\mathrm{m}}{\mathrm{s}}$	$(1\text{–}44)\times10^{-1}$
$\widehat{W}_t$	Tank width	M	2×10^{-1}
$\widehat{\mu}_\mathrm{a}$	Ambient fluid's viscosity	Pa s	1×10^{-3}
$\widehat{\mu}_\mathrm{j}$	Jet fluid's viscosity	Pa s	1×10^{-3}
$\widehat{\rho}_\mathrm{a}$	Ambient fluid's density	$\frac{\mathrm{kg}}{\mathrm{m}^3}$	9.98×10^2
$\widehat{\rho}_\mathrm{j}$	Jet fluid's density	$\frac{\mathrm{kg}}{\mathrm{m}^3}$	$(9.98\text{–}11.50)\times10^2$

technique proves to be more appropriate compared to the unsupervised one, which focuses on pattern identifications without a specific prediction goal. With these considerations in mind, let us now present a brief overview of the five popular supervised learning algorithms employed in our study for the predictive modeling of buoyant jet characteristics, including LR, SVR, RF, KNN, and ANN (with a focus on multi-layer perceptron (MLP)). Note that the LR and ANN algorithms are employed to model multiple regression problems, i.e., the target vector contains two outputs in our case ($y_k = [\, L_m \quad \theta \,]$). On the other hand, the SVR, RF and KNN algorithms are employed to model simple regression problems with a single output target ($y_k = [\, L_m \,]$ or $[\, \theta \,]$).

LR determines the best linear relationship between input features and the output. The schematic diagram depicting the structure of the LR model is illustrated in Figure 2a. Considering a dataset $\{(x_k, y_k)\}_{k=1}^{N}$, where N samples have multiple feature vectors (x_k) and targets (y_k) with $k = 1, \ldots, N$, the objective is to simply construct a linear model (f) in the form of [42]:

$$f(x) = wx + b, \tag{3}$$

where w is the weight matrix and b is the bias vector. In our case, a kth sample has the feature vector $x_k = [\, \mathrm{Re} \quad \mathrm{Ar} \,]$ and the target vector $y_k = [\, L_m \quad \theta \,]$. The optimal parameters of the model (w^*, b^*) are determined by minimizing an appropriate objective function through the gradient descent algorithm [50]. One example of a commonly used objective function is the "mean squared error", which is a quadratic cost function (see Table 2). Before moving to more complex models, we use LR in this study as a simpler model, i.e., less prone to overfitting compared to non-linear models [42].

SVR extends "support vector machines", which perform classifications by finding the optimal hyperplane with largest margin using support vectors, modeled as a quadratic optimization problem with various loss functions [54]. SVR can handle continuous values by introducing the ξ-tube insensitivity region around the function, to approximate it with the hyperplane represented by support vectors. In this model, the test and training data are independent and identically distributed. A typical quadratic loss function is [54]:

$$L_\xi(y_k, f(x_k, w)) = \begin{cases} 0, & |y_k - f(x_k, w)| \le \xi; \\ (|y_k - f(x_k, w)| - \xi)^2, & \text{otherwise}, \end{cases} \tag{4}$$

where x is the feature matrix containing $x_k = [\, \mathrm{Re} \quad \mathrm{Ar} \,]$ for all the samples ($k = 1, \ldots, N$), and y is the target matrix (single output) having a row $y_k = [\, L_m \,]$ or $[\, \theta \,]$ for all the samples ($k = 1, \ldots, N$). To reduce overfitting, a regularization parameter may be also introduced in this model. To handle datasets that cannot be separated by a hyperplane in the original space, the space is transformed into a higher dimension, enabling linear separation by a hyperplane. This process, known as kernelization [55], frequently utilizes the radial basis function (RBF) kernel [56]:

$$K(x_k, x') = \exp\left(-\frac{\|x_k - x'\|^2}{2\sigma^2}\right), \tag{5}$$

which calculates the similarity between two vectors (i.e., x_k and x') in space. In Equation (5), $\|x_k - x'\|$ denotes the L^2 norm (Euclidean distance) between the two vectors x_k (the feature vector of the kth sample) and x' (centroid vector), and σ represents the standard deviation. SVR is computationally efficient and offers high accuracy and strong generalization ability, regardless of the input space dimensionality [54]. Figure 2b shows the general schematic diagram of the SVR model used in our work.

RF is an ensemble learning method that combines multiple decision tree models to make a prediction (see Figure 2c). RF uses a bagging technique and randomly selects features for each split in the learning process. The prediction for a test data point is the average of the predictions made by each of the n decision trees [57]:

$$f(x_k) = \frac{1}{n}\sum_{i=1}^{n} f_i(x_k), \tag{6}$$

where x_k is the feature vector for the kth sample and $f_i(x_k)$ represents the prediction of the ith decision tree out of the n decision trees that make up the ensemble. Note that RF is immune to overfitting due to its ensemble approach [58].

KNN is an instance-based method that uses the training examples for every prediction [59]. It requires the storage of the training data and finds the K closest training samples to a new data point x_k, outputting the average target value [58]:

$$f(x_k) = \frac{1}{K}\sum_{x_i \in N_K(x_k)} y_i, \tag{7}$$

where $N_K(x_k)$ is the neighbourhood defined by the K closest points to x_k (i.e., the feature vector of the kth sample) in the training set and closeness is measured using a distance function such as the Euclidean distance or cosine similarity. y_i is the target vector (single output), i.e., $[\, L_m \,]$ or $[\, \theta \,]$ in our work, corresponding to the ith neighbour of x_k. Increasing K reduces overfitting, but also reduces resolution at decision boundaries. While KNN can handle non-linearities, it has a high prediction time, lacks interpretability and is unable to perform feature selection [58]. The visual representation of the KNN model architecture is given in Figure 2d.

ANN is a machine learning model inspired by the human brain [60]. In this method, a perceptron with a single neuron takes inputs, computes a linear combination, and outputs with a sigmoid activation. Multiple neurons can be layered to form an MLP network, represented by the function [61]:

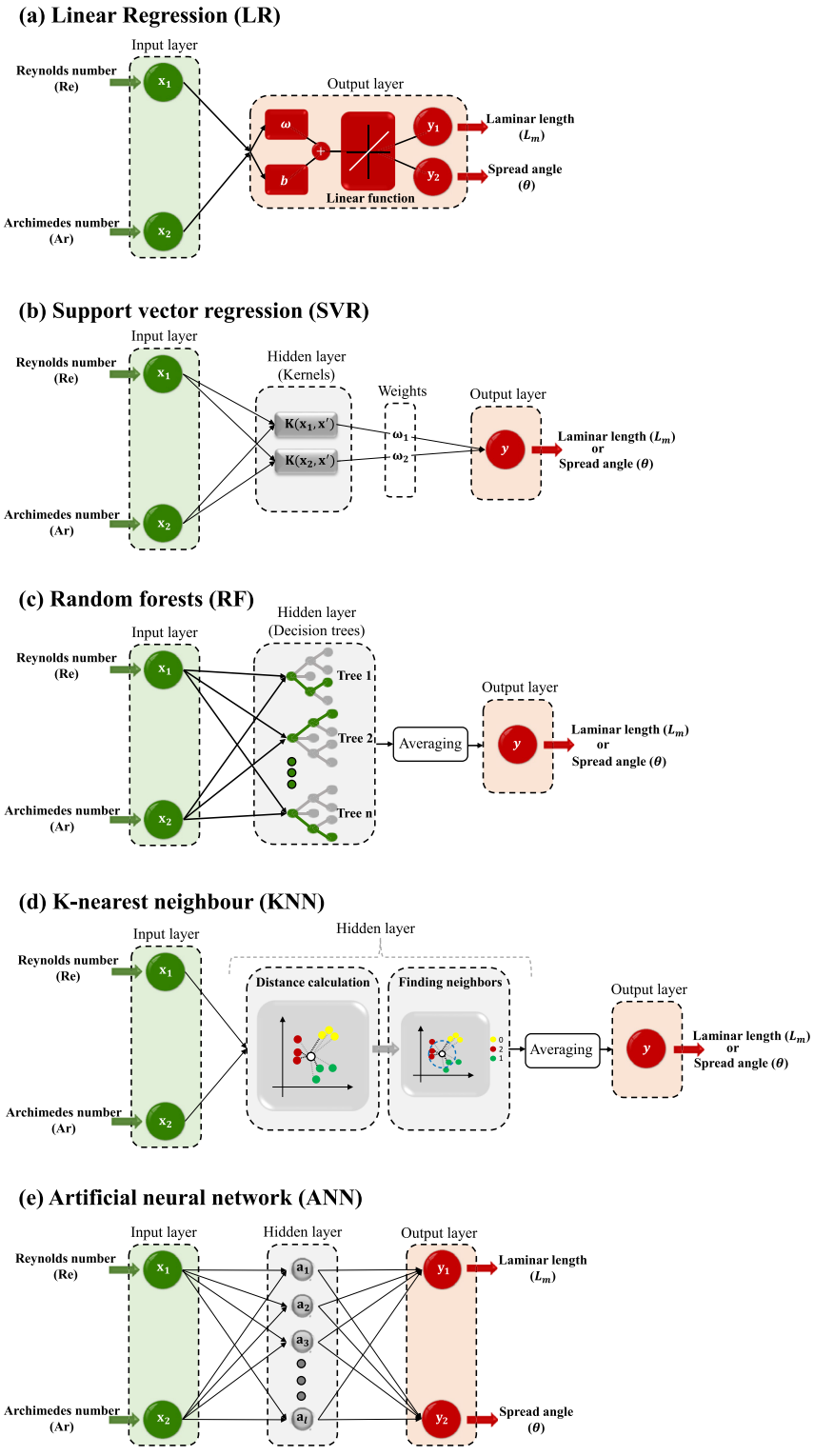

Figure 2: General architecture diagrams of different algorithms used in this study: (a) LR, (b) SVR, (c) RF, (d) KNN, and (e) ANN.

$$f(x) = f_l(f_{l-1}(\ldots(f_2(f_1(x))))). \tag{8}$$

with each layer having weights, biases and activation function assigned to it. The network is trained using gradient descent and back-propagation [62]. In addition, ANNs can capture complex patterns but require more data and computational resources than traditional algorithms [54]. Figure 2e illustrates the general architecture diagram of ANN model in our study.

Table 2: Mathematical formulation of different model performance metrics (y) [51–53], with $y_{i,\mathrm{o}}$ and $y_{i,\mathrm{p}}$ representing the observed and predicted values of the ith observations, respectively, and $\bar{y}$ being the mean value.

Name	Parameter	Mathematical formulation
Coefficient of determination	R^2	$\frac{\sum_i^N (y_{i,\mathrm{p}}-\bar{y})^2}{\sum_i^N (y_{i,\mathrm{o}}-\bar{y})^2}$
Mean squared error	MSE	$\frac{1}{N}\sum_i^N (y_{i,\mathrm{o}}-y_{i,\mathrm{p}})^2$
Root mean squared error	RMSE	$\sqrt{\frac{1}{N}\sum_i^N (y_{i,\mathrm{o}}-y_{i,\mathrm{p}})^2}$
Mean absolute error	MAE	$\frac{1}{N}\sum_i^N \lvert y_{i,\mathrm{o}}-y_{i,\mathrm{p}}\rvert$
Mean absolute percentage error	MAPE	$\frac{100}{N}\sum_i^N \lvert\frac{y_{i,\mathrm{o}}-y_{i,\mathrm{p}}}{y_{i,\mathrm{o}}}\rvert$

2.3 Models performance metrics

To evaluate the effectiveness of our machine learning models, we rely on standard performance metrics [63, 64], including coefficient of determination (R^2), mean squared error (MSE), root mean squared error (RMSE), mean absolute error (MAE), and mean absolute percentage error (MAPE). These standard metrics (listed in Table 2) provide a quantitative assessment of the model's performance and they are used to compare different models. For instance, MSE measures the average of the squares of the errors and incorporates both the estimator bias and variance. Also, RMSE is the square root of MSE and has the same units as the quantity being estimated. MAE does not assign importance to outliers. Finally, MAPE is similar to relative error and represents the average ratio of the difference between actual and predicted data. However, it may not be useful for data with low order of magnitudes (or close to zero) as it could lead to a surge in error.

Additionally, to understand the underlying linear relationships between the variables in the dataset, the linear correlation coefficient (r), taking values between –1 and +1, is used. A positive r would indicate that an increase in one variable is accompanied by an increase in another one, while a negative r would suggest a decrease in one variable as another one increases [65]. Therefore, r can provide insight into the relationship between our features and target variables.

3 Results and discussion

In this section, we first provide an overview of buoyant miscible jet characteristics via our experimental results. We then analyze and compare our trained machine learning models based on two jet flow features of interest (i.e., laminar length and spread angle) using multi-output target vectors for LR and ANN models, and single-output regression models for SVR, RF, and KNN. Finally, we examine the performance of RF in predicting of the jet's overall shape/boundary.

3.1 Buoyant miscible jet characteristics of interest

Let us present a typical experimental result of a heavy fluid (dark fluid) being vertically injected into a light ambient fluid (transparent fluid), as depicted in Figure 1b. The injection inertia and buoyancy forces combine to form a positively buoyant jet. At the initial portion of the jet, a stable column forms, without much obvious perturbation at the jet boundary. However, after a certain distance from the nozzle (i.e., the breakdown position), instabilities (e.g., Kelvin–Helmholtz type) cause the jet to become unstable, as evidenced by noticeable perturbations at the jet boundary, eventually resulting in mixing between the jet and ambient fluids. In the laminar length region, there is minimal mixing and the jet radius is roughly equal to the nozzle radius. On the other hand, beyond the breakdown position, the jet radius steadily increases, while the jet spread angle remains constant.

We also use PLIF to visualize the bottom-view of the jet, at varying axial distances from the nozzle. Figure 3a shows the equivalent dimensionless jet radius (defined as $r_{\mathrm{j}} = \sqrt{\frac{A}{\pi}}$ with A being the dimensionless jet cross-section area at a given time) versus time, at $X \approx 11$. This figure also includes three PLIF experimental images in the plane of

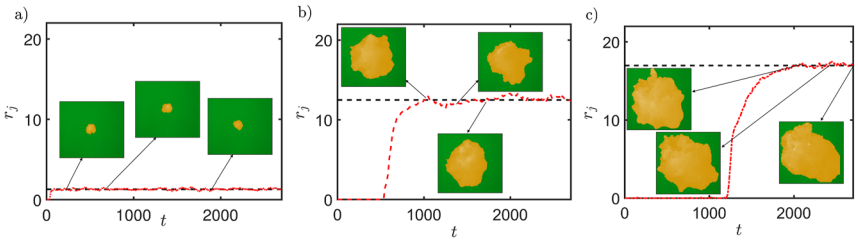

Figure 3: Development of jet radius over time at varying axial distances, (a) $X \approx 11$, (b) $X \approx 58$, (c) $X \approx 75$, as captured by PLIF (as exemplified by the superimposed experimental images), yielding a steady value indicated by black dashed line. The flow parameters are Re ≈ 4550 and Ar ≈ 41,703.

Y and Z. The jet radius increases initially and but it eventually reaches a quasi-steady value, i.e., not affected by further time progression. As the jet moves further away from the nozzle, as seen in Figure 3b ($X \approx 58$) and Figure 3c ($X \approx 75$), the jet radius increases and it takes more time for r_j to reach the quasi-steady value. Note that the zero value in the initial part of each plot represents the time required for the jet to reach the specific axial position for measurement.

3.2 Datasets

We use our experimental observations to create datasets to implement the machine learning algorithms, analyzing L_m and θ of our buoyant jets as functions of Re and Ar. Accordingly, we develop machine learning models for $\{L_m, \theta\}$ from feature vectors {Re, Ar}. To ensure that our machine learning models are robust and informative, we use a comprehensive set of experiments, i.e., 110 in total, covering a wide range of parameters. We divide the dataset into training and testing parts, specifically allocating 70 of these experiments as training datasets, with the remaining 40 used as test datasets, to validate the accuracy of our models. This approach enables us to create robust and reliable datasets that can provide valuable insights into the complex dynamics of our miscible buoyant jets. It is worth noting that the ranges of the dimensionless parameters for training and testing are $8 \times 10^2 \lesssim \text{Re} \lesssim 14 \times 10^3$ & $10^2 \lesssim \text{Ar} \lesssim 6 \times 10^5$. In addition, to decrease non-linearity and balance proportionality, we apply log transformation and standard scaling:

$$\zeta' = \frac{\log(\zeta) - \lambda_y}{\sigma}, \tag{9}$$

where ζ is the original (raw) data and ζ' is transformed data, while λ_y and σ are the mean and standard deviation of $\log(\zeta)$, respectively.

The tuning of hyper-parameters is an important piece of the machine learning puzzle that has a direct impact on the accuracy of the models [66]. In the literature, researchers have come up with various methods for finding the optimal hyper-parameters, ranging from sophisticated optimization algorithms, such as genetic algorithms and particle swarm optimization, to trial and error methods [66–68]. In the present study, the hyper-parameters are tuned employing the trial and error method, through a step-wise search approach. The optimal values for the hyper-parameters resulting from this procedure are presented in Table 3.

Before we proceed, it is worth briefly overviewing the smooth convergence of validation and training losses in ANN, as exemplified in Figure 4a and b; as seen, the training curve reaches the convergence loss faster while the validation loss decreases gradually. As the training continues these curves reach a stable state with a constant minimal gap, which is the optimal performance of ANN at which point the training process is terminated to prevent overfitting. Figure 4c and d give examples of the ANN model convergence, via plotting the experimental data versus the predicted data (i.e., $L_m^{\text{Exp.}}$ vs. $L_m^{\text{Pre.}}$ in Figure 4c, and $\theta^{\text{Exp.}}$ vs. $\theta^{\text{Pre.}}$ in Figure 4d). As epochs increase, the predicted values approach the experimental ones. However, as will be seen, the scarcity of data results in higher values of converged loss metrics in ANN compared to those in RF (see Table 4).

Table 3: The optimum values of the hyper-parameters for different algorithms.

Model	Hyper-parameters	
	L_m	θ
SVR	Margin of tolerance (ξ) = 0.05	Margin of tolerance (ξ) = 0.1
	Penalty parameter (C) = 1000	Penalty parameter (C) = 8
RF	Number of decision trees (n) = 200	Number of decision trees (n) = 200
KNN	Number of nearest neighbours (K) = 4	Number of nearest neighbours (K) = 2
ANN	Number of hidden layer (H) = 1	Number of hidden layer (H) = 1
	Number of neurons in the hidden layer (l) = 10	Number of neurons in the hidden layer (l) = 10

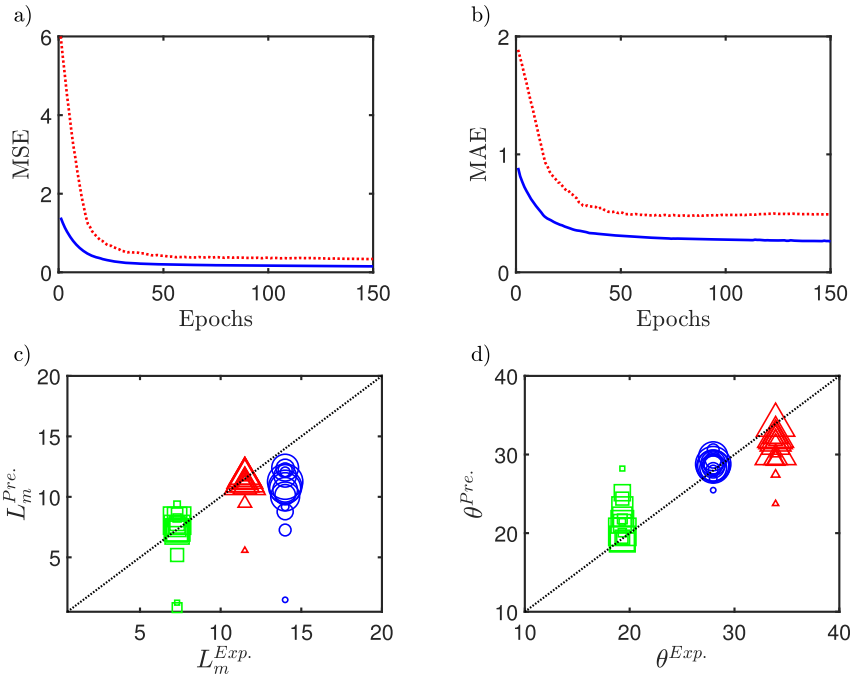

Figure 4: Loss plots for the training of ANN for (a) MSE and (b) MAE against the number of epochs (i.e., the number of times the gradient descent algorithm iterates over the entire training dataset), with the blue solid line representing training and the red dotted line representing validation. Variation of the positions of data points over increasing epochs in the plane of (c) $L_m^{Exp.}$ & $L_m^{Pre.}$, and (d) $\theta^{Exp.}$ & $\theta^{Pre.}$. The data correspond to Re ≈ 1500 & Ar ≈ 35,000 (blue circle), Re ≈ 1200 & Ar ≈ 450 (red triangle), and Re ≈ 3800 & Ar ≈ 296,000 (green square). The progressive increase in the symbol size indicates the increase in the corresponding epochs at an interval of 10. The dotted lines in (c) and (d) represent $L_m^{Exp.} = L_m^{Pre.}$ and $\theta^{Exp.} = \theta^{Pre.}$, respectively.

Table 4: Performance evaluation of models trained to predict L_m (first row for each model) and θ (second row for each model).

Algorithm	R^2	MSE	RMSE	MAE	MAPE
LR	0.89	2.85	1.69	0.91	23.04
	0.50	8.80	2.97	2.23	8.31
SVR	0.94	1.11	1.05	0.63	15.78
	0.84	3.02	1.74	1.26	4.63
RF	**0.96**	**0.80**	**0.89**	**0.54**	**13.73**
	0.91	**1.64**	**1.28**	**0.98**	**3.64**
KNN	0.90	1.96	1.40	0.96	24.35
	0.88	2.10	1.45	1.00	4.12
ANN	0.88	2.21	1.49	0.81	21.97
	0.70	5.35	2.310	1.72	6.46
Literature correlation [13]	0.84	6.16	2.48	1.89	23.96

The highlighted values in bold represent the most suitable choices for each parameter.

3.3 Laminar length (L_m)

The predictive modeling of the buoyant jet's laminar length (L_m), with Re and Ar as feature vectors, is depicted in Figure 5. As seen, L_m generally increases as Re decreases (which is evidenced by $r = -0.828$), yet shows little correlation with Ar (with $r \approx 0$); this can be also seen by the scattered distribution of L_m with respect to Ar. Almost all algorithms underestimate the laminar length at low Re, while showing better accuracy and uniformity at moderate Re. The goodness of the fit can be assessed through the proximity of the datapoints to the desired diagonal line $\left(L_m^{\text{Pre.}} = L_m^{\text{Exp.}}\right)$, with RF and SVR performing well, while LR and ANN showing lower accuracy. In addition, the KNN model performs properly but it risks overfitting to the training data.

We quantify the performance of the five models (i.e., LR, SVR, RF, KNN, and ANN) in terms of predicting the laminar length, by means of our five metrics described earlier (i.e., R^2, MSE, RMSE, MAE, and MAPE), as given in Table 4. As seen, LR and ANN have lower accuracy and R^2 values. On the other hand, RF outperforms the other models in terms of accuracy, i.e., indicated by its highest R^2 value, followed by SVR and KNN. RF also has the lowest error values, demonstrating its robustness, while a MAPE of less than 15 % further confirms its remarkable accuracy [69]. Note that RF even provides an improvement of 12 % over a recent empirical correlation in the literature [13] for L_m:

$$L_m \approx 324.4\left(\text{Ar}^{0.29} + 38.6\right)\text{Re}^{-1}. \tag{10}$$

3.4 Jet spread angle (θ)

Here, our aim is to predict the spread angle (θ) of our buoyant jets. Figure 6 compares the experimental and predicted θ for different values of Re and Ar. At low Re and Ar, the models tend to underestimate θ, evidenced by the negative correlations with Re ($r = -0.516$) and Ar ($r = -0.468$). More accurate models, such as RF and KNN, exhibit closer predictions to the desired diagonal line, while weaker models, such as LR and ANN, show discrepancies. This figure also reveals dependency of θ on Re, with lower (higher) θ at higher (lower) Re.

Let us also compare the performance of five algorithms using various metrics to predict θ. The results, shown in Table 4, demonstrate that RF has the best performance, indicated by its high R^2 value, while SVR and KNN have comparable results. RF outperforms the other models with a low MAPE of less than 4 %.

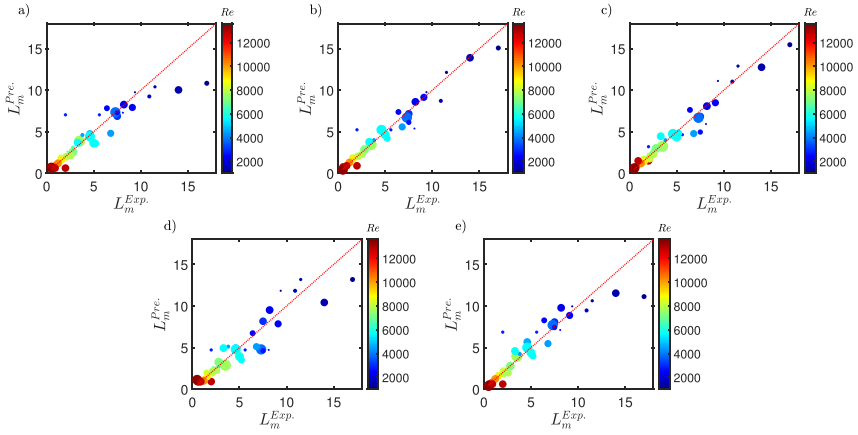

Figure 5: Variation of the predicted $\left(L_m^{\text{Pre.}}\right)$ and experimental $\left(L_m^{\text{Exp.}}\right)$ laminar lengths at different Re and Ar, based on (a) LR, (b) SVR, (c) RF, (d) KNN, and (e) ANN. The values of $8 \times 10^2 \lesssim \text{Re} \lesssim 14 \times 10^3$ and $10^2 \lesssim \text{Ar} \lesssim 6 \times 10^5$ are represented by the colors and the symbol sizes, respectively. The red dotted lines represent $L_m^{\text{Pre.}} = L_m^{\text{Exp.}}$.

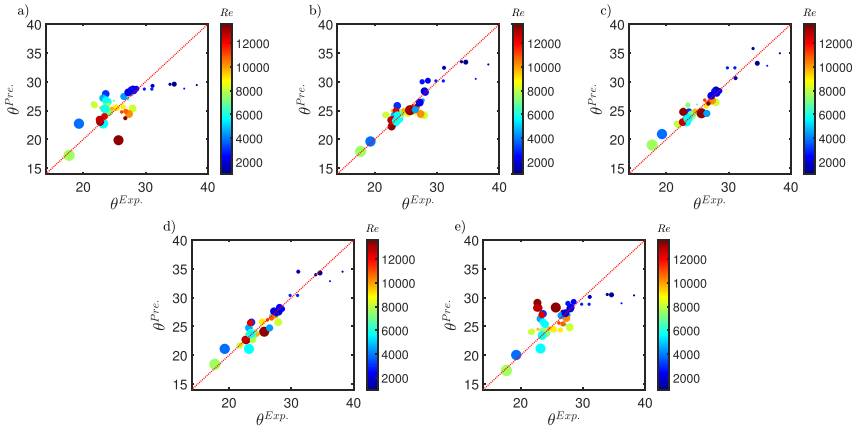

Figure 6: Comparison of predicted ($\theta^{Pre.}$) and experimental ($\theta^{Exp.}$) spread angle for different Re and Ar using five models: (a) LR, (b) SVR, (c) RF, (d) KNN, and (e) ANN, with the ideal case ($\theta^{Pre.} = \theta^{Exp.}$) represented by a red dotted line. The values of $8 \times 10^2 \lesssim \mathrm{Re} \lesssim 14 \times 10^3$ and $10^2 \lesssim \mathrm{Ar} \lesssim 6 \times 10^5$ are represented by the colors and the symbol sizes, respectively.

3.5 Jet shape

Accurately predicting both L_m and θ allows us to crudely describe the overall jet shape. As shown in Table 4, the RF algorithm surpasses the other models in accurately predicting both variables, with R^2 = 0.96 and MSE = 0.80 for L_m, and R^2 = 0.91 and MSE = 1.64 for θ. In addition, SVR with RBF kernel performs well in capturing non-linearity with R^2 = 0.94 and R^2 = 0.84 for L_m and θ, respectively. KNN also performs reasonably with R^2 = 0.90 and R^2 = 0.88 for L_m and θ, respectively, but may over-fit the data. Furthermore, both the ANN and LR models exhibit weak predictive capabilities for both the laminar length and spread angle, resulting in the lowest R^2 values. The inadequacy of ANN's performance can be attributed to the lack of a large training dataset, whereas LR's weak performance may be due to the inability of linear models to effectively approximate non-linear datasets. Overall, RF proves to be the best choice for our prediction tasks for both L_m and θ, thus, allowing us to crudely identify the jet overall shape.

Jet cross-sectional shapes are shown in Figure 7 for Re = 4550 and Ar = 41,703 at X = 11, X = 58, X = 75. The RF algorithm accurately captures the shape while the LR algorithm presents inconsistencies; this highlights the superiority of the RF algorithm in predicting the shape of our buoyant jets. To complement these results, Figure 8 presents a comparison between the three-dimensional jet boundaries obtained from experimental analysis and the RF model prediction, showing reasonable agreement. This finding highlights the remarkable accuracy of the RF model and its potential as a robust and reliable tool for predicting buoyant jet characteristics in different conditions.

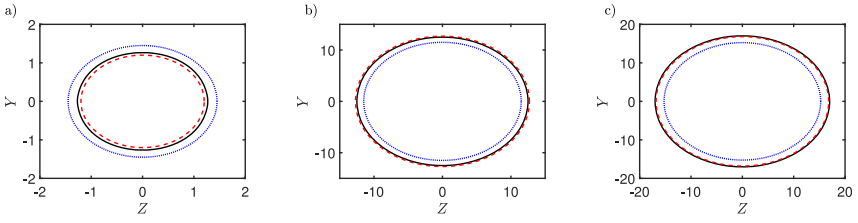

Figure 7: Jet cross-sectional shape in the Y–Z plane at (a) X = 11, (b) X = 58, and (c) X = 75, with data from experiment (black line), RF (red dashed line), and LR (blue dotted line). The flow parameters are Re ≈ 4550 and Ar ≈ 41,703.

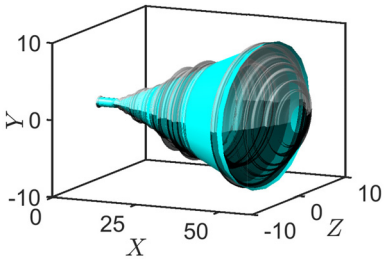

Figure 8: Three-dimensional jet boundaries obtained via the experiment (grey color) and RF model (cyan color), made via plotting the equivalent dimensionless jet radius in the axial direction. The flow parameters are Re ≈ 3800 and Ar ≈ 15,700.

4 Summary

In this work, we have studied positively buoyant vertical jets through a combination of experiments (high-speed imaging and PLIF) and machine learning techniques. Via considering two critical jet flow features (i.e., laminar length, L_m, and the spread angle, θ), we have determined the overall shape of the jet, while presenting our results based on governing dimensionless numbers, i.e., Re and Ar. Using supervised learning algorithms, we have used the LR and ANN models as multiple regression problems, and the SVR, RF, and KNN models as simple regression problems, while evaluating algorithm performance using metrics such as R^2, MSE, RMSE, MAE, and MAPE. The RF algorithm has shown excellent consistency with the experimental data, producing the best model performance, even outperforming prior empirical correlations ([13]) by 12 % in accuracy. Our study may lay the foundation for future research avenues, including predicting negatively buoyant jet shapes, incorporating viscosity ratios, exploring non-Newtonian fluids, and utilizing deep learning techniques for higher accuracy and efficiency. This can eventually lead to optimizing and controlling buoyant jets in practical applications.

Nomenclature

$\widehat{D}_n$	Nozzle diameter
$\widehat{g}$	Gravitational acceleration
$\widehat{L}_t$	Setup length
$\widehat{V}_0$	Injection velocity
$\widehat{W}_t$	Setup width
A	Jet cross-section area
ANN	Artificial neural network
Ar	Archimedes number
b	Bias vector
C	Penalty parameter in SVR
H	Number of hidden layers in ANN
K	Nearest neighbours in KNN
k	Index
KNN	K-nearest neighbour
l	Number of neurons in the hidden layer
L_m	Laminar length
LR	Linear regression
MAE	Mean absolute error
MAPE	Mean absolute percentage error
MLP	Multi-layer perceptron
MSE	Mean squared error
N	Number of samples
n	Number of decision trees
PLIF	Planar laser-induced fluorescence
r	Linear correlation coefficient
R^2	Coefficient of determination
r_j	Jet radius

RBF	Radial basis function
Re	Reynolds number
RF	Random forest
RMSE	Root mean squared error
SVR	Support vector regression
t	time
X	Axial coordinate
x	Feature vector
Y	Transverse coordinate
y	Target vector
Z	Depth coordinate
λ	Mean deviation
μ	Viscosity
ω	Weight matrix
ρ	Density
σ	Standard deviation
θ	Spread angle
ξ	Margin of tolerance in SVR
ζ	Original data
ζ'	Transformed data

Acknowledgement: The authors would like to thank Mr. R. Mahmoudi for his valuable comments.
Author contribution: All the authors have accepted responsibility for the entire content of this submitted manuscript and approved submission.
Research funding: This research has been carried out at Université Laval. The authors wish to acknowledge the financial support of this research by PTAC-AUPRF via Grant No. AUPRF2022-000124 and NSERC via Alliance Grant No. ALLRP 577111-22 ("Towards Net-Zero Emissions: mechanics, processes and materials to support risk-based well decommissioning"). The authors also express their gratitude to the Natural Sciences and Engineering Research Council of Canada, via the Discovery Grant (Grant No. CG109154) and Research Tools and Instruments Grant (Grant No. CG132931), the Canada Research Chair on Modeling Complex Flows (Grant No. CG125810), and the Canada Foundation for Innovation via the John R. Evans Leaders Fund (Grant No. GF130120, GQ130119 and GF525075). SJ also acknowledges the Mitacs Globalink Research Internship Award.
Conflict of interest statement: The authors declare no conflicts of interest regarding this article.

References

1. Dadonau M, Partridge JL, Linden PF. The effect of double diffusion on the dynamics of horizontal turbulent thermohaline jets. J Fluid Mech 2020;905:1–20.
2. Hassanzadeh H, Eslami A, Taghavi SM. On the role of the viscosity ratio on buoyant miscible jet flows. Environ Fluid Mech 2022;22:337–65.
3. Hunt GR, Burridge HC. Fountains in industry and nature. Annu Rev Fluid Mech 2015;47:195–220.
4. Apsley DD, Lane-Serff GF. Collapse of particle-laden buoyant plumes. J Fluid Mech 2019;865:904–27.
5. Rodríguez-Benítez AJ, Álvarez-Díaz C, García-Gómez A, García-Alba J. Methodological approaches for delimitating mixing zones in rivers: establishing admissibility criteria and flow regime representation. Environ Fluid Mech 2018;18:1227–56.
6. Hauchecorne A. Jet-setting atmosphere. Nat Geosci 2017;10:622–3.
7. Stevens B. Atmospheric moist convection. Annu Rev Earth Planet Sci 2005;33:605–43.
8. Robinson D, Wood M, Piggott M, Gorman G. CFD modelling of marine discharge mixing and dispersion. J Appl Water Eng Res 2016;4: 152–62.
9. Gharavi A, Mohammadian A, Nistor I, Peña E, Anta J. Experimental study of surface buoyant jets in crossflow. Environ Fluid Mech 2020;20: 1007–30.
10. Landel JR, Wilson DI. The fluid mechanics of cleaning and decontamination of surfaces. Annu Rev Fluid Mech 2021;53:147–71.
11. Hassanzadeh H, Cournoyer E, Taghavi SM. Jet cleaning processes in the plug and abandonment of oil and gas wells: an experimental study on horizontal miscible jets. In: International conference on offshore mechanics and arctic engineering. American Society of Mechanical Engineers; 2022, vol 85956:V010T11A055 p.

12. Liu X, Liu X, Zhang T. Influence of air-conditioning systems on buoyancy driven air infiltration in large space buildings: a case study of a railway station. Energy Build 2020;210:109781.
13. Hassanzadeh H, Eslami A, Taghavi SM. Positively buoyant jets: semiturbulent to fully turbulent regimes. Phys Rev Fluids 2021;6:054501.
14. Panigrahi PK, Muralidhar K. Imaging jet flow patterns. In: Imaging heat and mass transfer processes: visualization and analysis; 2013: 101–29 pp.
15. Kitamura S, Sumita I. Experiments on a turbulent plume: shape analyses. J Geophys Res Solid Earth 2011;116:1–15.
16. Pantzlaff L, Lueptow RM. Transient positively and negatively buoyant turbulent round jets. Exp Fluid 1999;27:117–25.
17. Talluru KM, Armfield S, Williamson N, Kirkpatrick MP, Milton-McGurk L. Turbulence structure of neutral and negatively buoyant jets. J Fluid Mech 2021;909:A14.
18. McNaughton KJ, Sinclair CG. Submerged jets in short cylindrical flow vessels. J Fluid Mech 1966;25:367–75.
19. Sreenivas KR, Prasad AK. Vortex-dynamics model for entrainment in jets and plumes. Phys Fluids 2000;12:2101–7.
20. Mollendorf JC, Gebhart B. An experimental and numerical study of the viscous stability of a round laminar vertical jet with and without thermal buoyancy for symmetric and asymmetric disturbances. J Fluid Mech 1973;61:367–99.
21. Lemanov VV, Terekhov VI, Sharov KA, Shumeiko AA. An experimental study of submerged jets at low Reynolds numbers. Tech Phys Lett 2013;39:421–3.
22. Munwes YY, Geyer S, Katoshevski D, Ionescu D, Licha T, Lott C, et al. Discharge estimation of submarine springs in the dead sea based on velocity or density measurements in proximity to the water surface. Hydrol Process 2020;34:455–72.
23. Gao F, Zhao L, Boufadel MC, King T, Robinson B, Conmy R, et al. Hydrodynamics of oil jets without and with dispersant: experimental and numerical characterization. Appl Ocean Res 2017;68:77–90.
24. Werner RA, Geier DU, Becker T. The challenge of cleaning woven filter cloth in the beverage industry-wash jets as an appropriate solution. Food Eng Rev 2020;12:520–45.
25. Rengel B, Àgueda A, Pastor E, Casal J, Planas E, Hu L, et al. Experimental and computational analysis of vertical jet fires of methane in normal and sub-atmospheric pressures. Fuel 2020;265:116878.
26. Chojnicki KN, Clarke AB, Phillips JC, Adrian RJ. The evolution of volcanic plume morphology in short-lived eruptions. Geology 2015;43: 707–10.
27. Malcangio D, Cuthbertson A, Meftah MB, Mossa M. Computational simulation of round thermal jets in an ambient cross flow using a large-scale hydrodynamic model. J Hydraul Res 2020;58:920–37.
28. Miyazaki Y, Usawa M, Kawai S, Yee J, Muto M, Tagawa Y. Dynamic mechanical interaction between injection liquid and human tissue simulant induced by needle-free injection of a highly focused microjet. Sci Rep 2021;11:1–10.
29. Chen F, Lan C. Fabrication of elastomeric microfluidic channels based on light-curing electrostatic printing. Microfluid Nanofluidics 2022; 26:84.
30. Zeng D, Wu N, Xie L, Xia X, Kang Y. An experimental study of a spring-loaded needle-free injector: influence of the ejection volume and injector orifice diameter. J Mech Sci Technol 2019;33:5581–8.
31. Géron A. Hands-on machine learning with scikit-learn and tensorflow. Tools, and techniques to build intelligent systems. Sebastopol, CA, USA: O'Reilly Media; 2017.
32. Sarker IH. Deep learning: a comprehensive overview on techniques, taxonomy, applications and research directions. SN Comput Sci 2021; 2:420.
33. Artrith N, Butler KT, Coudert F, Han S, Isayev O, Jain A, et al. Best practices in machine learning for chemistry. Nat Chem 2021;13:505–8.
34. Rasku J. Toward automatic customization of vehicle routing systems [JYU dissertations]; 2019.
35. Alashwal H, El Halaby M, Crouse JJ, Abdalla A, Moustafa AA. The application of unsupervised clustering methods to Alzheimer's disease. Front Comput Neurosci 2019;13:31.
36. Sindhu Meena K, Suriya S. A survey on supervised and unsupervised learning techniques. In: Proceedings of international conference on artificial intelligence, smart grid and smart city applications: AISGSC 2019. Springer; 2020:627–44 pp.
37. Patel K, Patel HB. A comparative analysis of supervised machine learning algorithm for agriculture crop prediction. In: 2021 Fourth international conference on electrical, computer and communication technologies (ICECCT). IEEE; 2021:1–5 pp.
38. Cord M, Cunningham P. Machine learning techniques for multimedia: case studies on organization and retrieval. Berlin, Heidelberg: Springer; 2008.
39. Pruneski JA, Pareek A, Kunze KN, Martin RK, Karlsson J, Oeding JF, et al. Supervised machine learning and associated algorithms: applications in orthopedic surgery. Knee Surg Sports Traumatol Arthrosc 2023;31:1196–202.
40. Brunton SL, Noack BR, Koumoutsakos P. Machine learning for fluid mechanics. Annu Rev Fluid Mech 2020;52:477–508.
41. Tiwari A. Supervised learning: from theory to applications. In: Artificial intelligence and machine learning for EDGE computing. Amsterdam: Elsevier; 2022.
42. Burkov A. The hundred-page machine learning book. QC, Canada: Burkov; 2019, 1.
43. Alloghani M, Al-Jumeily D, Mustafina J, Hussain A, Aljaaf AJ. A systematic review on supervised and unsupervised machine learning algorithms for data science. In: Supervised and unsupervised learning for data science. Cham, Switzerland: Springer; 2020:3–21 pp.
44. Kulikov A, Loskutov A, Bezdushniy D. Relay protection and automation algorithms of electrical networks based on simulation and machine learning methods. Energies 2022;15:6525.
45. Dang W, Guo J, Liu M, Liu S, Yang B, Yin L, et al. A semi-supervised extreme learning machine algorithm based on the new weighted kernel for machine smell. Appl Sci 2022;12:9213.

46. Hong N, Liu C, Gao J, Han L, Chang F, Gong M, et al. State of the art of machine learning–enabled clinical decision support in intensive care units: literature review. JMIR Med Inform 2022;10:e28781.
47. El-Amin MF, Subasi A. Predicting turbulent buoyant jet using machine learning techniques. In: 2020 2nd International conference on computer and information sciences (ICCIS). IEEE; 2020:1–5 pp.
48. Mashhadimoslem H, Ghaemi A, Palacios A, Almansoori A, Elkamel A. Machine learning modeling and evaluation of jet fires from natural gas processing, storage, and transport. Can J Chem Eng 2023;1:1–13.
49. Kumar M, Tiwari NK, Ranjan S. Application of machine learning methods in estimating the oxygenation performance of various configurations of plunging hollow jet aerators. J Environ Eng 2022;148:04022070.
50. Oymak S, Soltanolkotabi M. Overparameterized nonlinear learning: gradient descent takes the shortest path? In: International conference on machine learning. PMLR; 2019:4951–60 pp.
51. Moghaddam SHA, Mokhtarzade M, Naeini AA, Amiri-Simkooei A. A statistical variable selection solution for RFM ill-posedness and overparameterization problems. IEEE Trans Geosci Rem Sens 2018;56:3990–4001.
52. Wallach D, Goffinet B. Mean squared error of prediction as a criterion for evaluating and comparing system models. Ecol Model 1989;44: 299–306.
53. Shcherbakov MV, Brebels A, Shcherbakova NL, Tyukov AP, Janovsky TA, Kamaev VA. A survey of forecast error measures. World Appl Sci J 2013;24:171–6.
54. Awad M, Khanna R. Support vector regression. In: Efficient learning machines: theories, concepts, and applications for engineers and system designers. New York, NY, USA: Springer Nature; 2015:67–80 pp.
55. Fernandes SEN, Pilastri AL, Pereira LAM, Pires RG, Papa JP. Learning kernels for support vector machines with polynomial powers of sigmoid. In: 2014 27th SIBGRAPI conference on graphics, patterns and images. IEEE; 2014:259–65 pp.
56. Ding X, Liu J, Yang F, Cao J. Random radial basis function kernel-based support vector machine. J Franklin Inst 2021;358:10121–40.
57. Cutler A, Cutler DR, Stevens JR. Random forests. In: Ensemble machine learning: methods and applications. New York, NY, USA: Springer; 2012:157–75 pp.
58. Hastie T, Tibshirani R, Friedman JH, Friedman JH. The elements of statistical learning: data mining, inference, and prediction. New York, NY: Springer; 2009, 2.
59. Chen J, Huang H, Hsu C. A KNN based position prediction method for SNS places. In: Intelligent information and database systems: 12th Asian conference, ACIIDS 2020, Phuket, Thailand, March 23–26, 2020, proceedings, part II 12. Springer; 2020:266–73 pp.
60. Kim M, Yun J, Cho Y, Shin K, Jang R, Bae H, et al. Deep learning in medical imaging. Neurospine 2020;17:471.
61. Joshi AV. Perceptron and neural networks. In: Machine learning and artificial intelligence. Switzerland: Springer; 2022:57–72 pp.
62. Panerati J, Schnellmann MA, Patience C, Beltrame G, Patience GS. Experimental methods in chemical engineering: artificial neural networks-ANNs. Can J Chem Eng 2019;97:2372–82.
63. Hoffmann F, Bertram T, Mikut R, Reischl M, Nelles O. Benchmarking in classification and regression. Wiley Interdiscip Rev: Data Min Knowl Discov 2019;9:e1318.
64. Kioumarsi M, Dabiri H, Kandiri A, Farhangi V. Compressive strength of concrete containing furnace blast slag; optimized machine learning-based models. Clean Eng Technol 2023;13:100604.
65. Ratner B. The correlation coefficient: its values range between +1/−1, or do they? J Target Meas Anal Market 2009;17:139–42.
66. Behnam P, Faegh M, Shafii MB, Khiadani M. A comparative study of various machine learning methods for performance prediction of an evaporative condenser. Int J Refrig 2021;126:280–90.
67. Maier HR, Jain A, Dandy GC, Sudheer KP. Methods used for the development of neural networks for the prediction of water resource variables in river systems: current status and future directions. Environ Model Software 2010;25:891–909.
68. Rojas-Domínguez A, Padierna LC, Valadez MC, Juan, Puga-Soberanes HJ, Fraire HJ. Optimal hyper-parameter tuning of SVM classifiers with application to medical diagnosis. IEEE Access 2017;6:7164–76.
69. Chen HC, Chen WJ, Zhou Y. Estimation of chromaticity coordinates for LEDs array by modulation of red or yellow LEDs with artificial neural network. In: 2013 Ninth international conference on intelligent information hiding and multimedia signal processing. IEEE; 2013: 88–91 pp.